PCCP

PAPER

View Article Online
View Journal | View Issue

Cite this: *Phys. Chem. Chem. Phys.*, 2016, **18**, 4008

Deconstructing field-induced ketene isomerization through Lagrangian descriptors

Galen T. Craven* and Rigoberto Hernandez*

Received 30th October 2015,
Accepted 1st January 2016

DOI: 10.1039/c5cp06624g

www.rsc.org/pccp

The time-dependent geometrical separatrices governing state transitions in field-induced ketene isomerization are constructed using the method of Lagrangian descriptors. We obtain the stable and unstable manifolds of time-varying transition states as dynamic phase space objects governing configurational changes when the ketene molecule is subjected to an oscillating electric field. The dynamics of the isomerization reaction are modeled through classical trajectory studies on the Gezelter–Miller potential energy surface and an approximate dipole moment model which is coupled to a time-dependent electric field. We obtain a representation of the reaction geometry, over varying field strengths and oscillation frequencies, by partitioning an initial phase space into basins labeled according to which product state is reached at a given time. The borders between these basins are in agreement with those obtained using Lagrangian descriptors, even in regimes exhibiting chaotic dynamics. Major outcomes of this work are: validation and extension of a transition state theory framework built from Lagrangian descriptors, elaboration of the applicability for this theory to periodically- and aperiodically-driven molecular systems, and prediction of regimes in which isomerization of ketene and its derivatives may be controlled using an external field.

A purely geometrical picture of a chemical reaction, when available, can represent the most pertinent current understanding of the dynamics governing state transitions in activated events. For example, transition state theory (TST) and its variants constitute the most popular of the modern methods for prediction of chemical reaction rates. These theories rely on geometric information alone, requiring only knowledge of the respective potential energy surface to allow calculation of the rates of dynamical processes. As such, TST is a pillar of reaction dynamics and kinetics.[1–8] In activated events, the interplay between rates and mechanisms of conversion from reactants to products can be controlled so as to bias the reactivity and selectivity of a reaction toward products of interest. The principal geometric structures needed to understand these conversions are invariant manifolds (reaction conduits) which form separatrices that distinguish between states.

In isolated Hamiltonian systems with two degrees of freedom, the relevant reaction dynamics can be understood through the unstable periodic orbit dividing surface (PODS) that separates reactant and product states.[9–12] At higher dimensionality, the PODS can be generalized to a normally hyperbolic invariant manifold (NHIM).[8,13–21] A NHIM has associated reaction cylinders (stable and unstable manifolds) in isolated systems at energies below bifurcation thresholds.[22–25] Moreover, reactive events are mediated by these manifolds[26] on (sometimes bifurcating[27]) reaction pathways attached to the NHIM. Thus, NHIMs are a powerful methodological tool for characterizing reactive events in Hamiltonian systems that are autonomous, that is conservative systems that are not subject to time-dependent forces.

In the case of thermally-activated[28–30] and field-induced reactions:[31–35] time-dependent normal form theory,[36,37] scattering theories,[38,39] and high-order perturbation theories[40,41] have provided insight into the geometric structure of externally-activated processes. Control of state transitions in dynamical systems[42–44] can be achieved in nonstatistical processes,[45] including those with fluctuating rates.[33,34,46,47] To overcome the intrinsic complexity in these mechanisms, theories built on stability analysis[48–51] of guiding phase space objects have been developed.[33,34,52,53] Of specific interest in this class of driven reactions are recent advances in the control of protein dynamics using lasers[54,55] and mechanical stress.[56] Theories that describe the time-dependent geometry of such systems provide a method to obtain and manipulate the rate of transition in these, and other, time-dependent processes.

Recently, a method relying on the construction of a Lagrangian descriptor (LD)[57] has been proposed to reveal phase objects such as hyperbolic trajectories[58,59] and invariant manifolds. This methodology relies on computation and comparison of the arc lengths in forward and backward time for sets of trajectories with initial conditions in regions of phase space that are relevant to the system dynamics. The measure of these LDs can vary greatly on each side of a phase space boundary and their

Center for Computational Molecular Science and Technology, School of Chemistry and Biochemistry, Georgia Institute of Technology, Atlanta, GA, USA.
E-mail: gtcraven@gatech.edu, hernandez@gatech.edu

application to time-dependent systems has provided insight into the structures governing dynamical evolution in ocean flow patterns[57] and other systems modulated by external fields.[60] In thermal environments, the mechanisms and intrinsic reaction conduits that drive time-dependent reactive phenomena can also be described by this methodology.[61]

Our focus here is to develop a theory for reaction dynamics in field-induced systems through application of LDs using isomerization of ketene as a model system. Specifically, a time-dependent field is applied to the ketene molecule for which the time-dependent manifolds and hyperbolic trajectories governing reactivity are revealed through LDs. The gas-phase (isolated) ketene isomerization reaction has received attention both as a model to investigate geometrical properties[62–65] and for its physical importance to chemical processes such as the Wolff rearrangement.[66–68] It is also a paradigmatic example reaction for the chemical control of interest to this work because field-modified reactivity of ketene has been observed.[69,70] To illustrate the methodology, we construct the network of manifolds over varying field strengths and oscillation frequencies. At select field parameters we observe the onset of chaos, as characterized by entanglement of these manifolds. The results provide insight into the treatment of field-induced reaction dynamics and other activated events driven under dynamical load.

1 Model and simulation details

The isomerization of ketene:

$$H_2C^1{=}C^2{=}O \rightleftharpoons O{=}C^1{=}C^2H_2 \quad (1)$$

proceeds through metastable oxirene and formylmethylene intermediates which participate in the generally accepted mechanism for the Wolff rearrangement.[68,71] Using the structural calculations of Scott *et al.*,[68] Gezelter and Miller (GM) constructed a model potential energy surface for this unimolecular reaction.[72] They identified normal and local modes associated with the coupled in-plane motion of O and H atoms as the principal reaction coordinate (q_1), and the out-of-plane vibration of the H atom in oxirene as a secondary coordinate (mode q_2).[62,63,72] The potential of the multi-dimensional GM surface is

$$V(q_1,q_2) = V_1(q_1) + V_{\text{coup}}(q_1,q_2), \quad (2)$$

which contains a one-dimensional term (see Fig. 1) along the fundamental reaction coordinate q_1

$$V_1(q_1) = a_2{q_1}^2 + a_4{q_1}^4 + a_6{q_1}^6 + c{q_1}^2 e^{-d{q_1}^2}, \quad (3)$$

and a coupling term

$$V_{\text{coup}}(q_1,q_2) = \frac{k_1}{2}\left(q_2 + \frac{d_1{q_1}^4}{k_1}\right)^2. \quad (4)$$

A projection of the GM potential onto the $q_1 \times q_2$ plane is shown in Fig. 1 and the system parameters are given in Table 1. Using the GM potential, we develop two separate models (I and II) for field-induced ketene isomerization: in Model I, the coupling term V_{coup} is ignored and an effective two-dimensional phase space is constructed by setting $k_1 = 0$. Model II is a four dimensional phase space model, constructed by including the coupling term and generalized velocity of mode q_2.

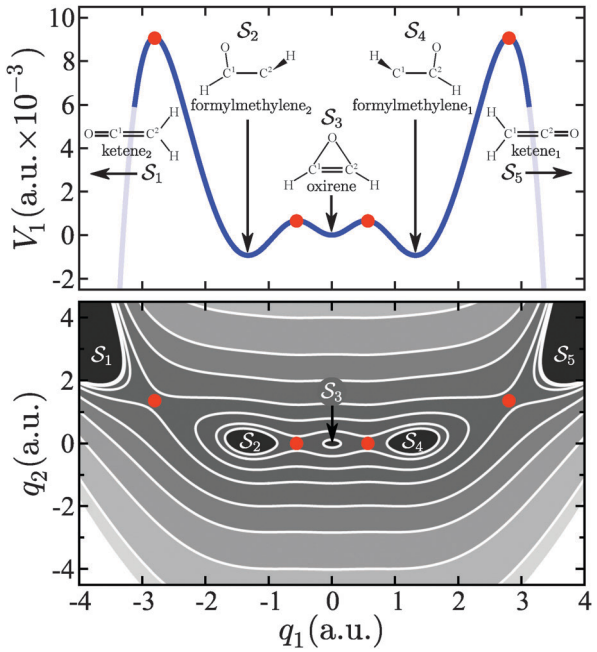

Fig. 1 The GM potential and corresponding structures for ketene isomerization along the principal reaction coordinate q_1 are shown in the top panel and a contour plot of the multidimensional surface in the $q_1 \times q_2$ plane is shown below. The position of each TS is shown as a circular marker (red) and each stable-state basin S_k is labeled.

Table 1 Parameters of the GM potential

Parameter	Value
a_2	-2.3597×10^{-3} ($E_h a_0^{-2}$)
a_4	1.0408×10^{-3} ($E_h a_0^{-4}$)
a_6	-7.5496×10^{-5} ($E_h a_0^{-6}$)
c	7.7569×10^{-3} ($E_h a_0^{-2}$)
d	1.9769 (a_0^{-2})
k_1 (Model I)	0 ($E_h a_0^{-2}$)
k_1 (Model II)	1.0074×10^{-2} ($E_h a_0^{-2}$)
d_1	-2.45182×10^{-4} ($E_h a_0^{-5}$)

Four transition states (TS) exist along the fundamental reaction coordinate q_1: the inner TSs ($q_1 = \pm 0.5467\ a_0$) which separate the oxirene–formylmethylene stable basins, and the outer TSs ($q_1 = \pm 2.8047\ a_0$) which separate the formylmethylene–ketene basins. The indices of these TSs used herein is given in Table 2. Further stability analysis of the TSs can be found in ref. 65. The barrier separating oxirene and the inner TS has an activation energy $\Delta V = 0.00067$ a.u. and the formylmethylene to outer TS barrier has a larger activation barrier of $\Delta V = 0.010$ a.u. and thus formylmethylene is correspondingly the most stable of the two metastable structures.

Ketene is active in electric fields and susceptible to field-induced reactivity studies.[69,70] We will approximate the field-matter interaction of ketene with a classical dipole approximation.

Table 2 Positions of TSs along the fundamental reaction coordinate q_1

Transition state	Position
TS_1 (outer)	-2.8047 (a_0)
TS_2 (inner)	-0.5467 (a_0)
TS_3 (inner)	0.5467 (a_0)
TS_4 (outer)	2.8047 (a_0)

To construct a dipole function, the geometry of each TS and stable-basin structure was taken from ref. 68 in which Scott *et al.* performed electronic structure calculations at the CCSD(T)/6-311G(*df,p*) level. Using these geometries, the dipole moment of each was computed by employing a B3LYP/6-311+G** scheme. The results of these calculations are shown in Table 3. The dipole moment along q_1 is modeled through an approximation of the form

$$\mu_m(q_1) = \mu_0\left[\exp\left(-\alpha(q_1 - q_0)^4\right)\right] + \mu_0\left[\exp\left(-\alpha(q_1 + q_0)^4\right)\right] + \mu_{\text{ketene}}. \quad (5)$$

where we assume that out-of-plane hydrogen motion in oxirene (q_2) has a negligible effect on the dipole moment in the pertinent dynamical regions and about the minimum energy pathway. The best-fit parameters for eqn (5) were obtained from least-squares regression to the calculated dipole moments, yielding $\mu_0 = 0.546\ ea_0$, $\alpha = 0.0701\ a_0^{-4}$, $q_0 = 1.95\ a_0$, and $\mu_{\text{ketene}} = 0.602\ ea_0$. A comparison between the results given by the model dipole moment surface μ and the computational results can be found in Table 3.

With the potential energy and dipole moment surfaces now defined, the molecular Lagrangian for ketene can be written as

$$\mathscr{L} = \frac{1}{2}m_f\dot{q}_1^2 + \frac{1}{2}m_H\dot{q}_2^2 - V_1(q_1) - V_{\text{coup}}(q_1, q_2) + \mathscr{E}(t)\mu_m(q_1), \quad (6)$$

leading to the equations of motion

$$m_f\ddot{q}_1 = -\frac{dV_1}{dq_1} - \frac{\partial V_{\text{coup}}}{\partial q_1} + \mathscr{E}(t)\frac{d\mu_m}{dq_1}, \quad (7a)$$

$$m_H\ddot{q}_2 = -\frac{\partial V_{\text{coup}}}{\partial q_2}, \quad (7b)$$

where $\mathscr{E}(t)$ is the applied electric field. Associated with each coordinate (q_1,q_2) is the corresponding generalized velocity and thus the dynamics is either two dimensional (Model I) or four dimensional (Model II) with each phase space point represented by $\mathbf{q} = (q_1,\dot{q}_1)$ or $\mathbf{q} = (q_1,\dot{q}_1,q_2,\dot{q}_2)$, respectively. A constant-mass approximation associated with the corresponding normal mode of the oxirene intermediate has been calculated as $m_f = 9581$ in atomic units (a.u.).[63] The mass of the out-of-plane oxirene stretch mode is $m_H = 1837$ a.u.,[63,65,72] the mass of hydrogen. The chosen field takes the sinusoidal form $\mathscr{E}(t) = \mathscr{E}_0\sin(\omega t + \phi)$ where $\mathscr{E}_0$ is the field strength, ω is the oscillation frequency, and ϕ is the phase which is held constant ($\phi = \pi$). We investigate field strengths in range of those used previously in studies of field-induced diatomic chemical reactions,[75] and also strengths in range of ionization thresholds. The frequencies studied are below $\omega = 0.2$ a.u. (230 nm), a value previously used in experimental analysis of the decomposition of ketene.[70] Throughout this study, the integration of eqn (7a) and (7b) is performed using a Runga–Kutta fourth-order scheme with a time-step $\Delta t = 0.1$ (atomic units).

Table 3 Dipole moments of various structures in ketene isomerization. All values are reported in atomic units

Structure	Computation	μ_m	Experiment
Oxirene	1.01	1.00	—
Inner TS	1.05	1.05	—
Formylmethylene	1.09	1.14	—
Outer TS	1.18	1.13	—
Ketene ($q_1 = 4.5\ a_0$)	0.602	0.630	—
Ketene ($\lim q_1 \to \infty$)	0.602	0.602	0.570 (ref. 73), 0.560 (ref. 74)

2 Lagrangian descriptors

The application of LDs to the study of time-dependent flows has ranged over systems as diverse as thermal chemical reactions,[61] human biomechanics,[76] and ocean flow patterns.[57] In the general formulation,[57,60] a LD can be expressed as

$$M(\mathbf{q}_0, t_0)_\tau = \int_{t_0-\tau}^{t_0+\tau} \mathscr{P}(\mathbf{q}(t))\mathrm{d}t, \quad (8)$$

where $\mathscr{P}$ is a bounded positive quantity and a functional of the trajectory $\mathbf{q}(t)$ with *initial* condition $\mathbf{q}_0$ at time t_0. The integration of this quantity is taken over the time interval $[t_0 - \tau, t_0 + \tau]$ and thereby includes information from both forward- and backward-time. Thus, a LD is a mapping from the phase space point $\mathbf{q}_0$ to the scalar value M using dynamical information obtained along a corresponding trajectory. The LDs corresponding to arc length measures in phase space and configuration space are useful for constructing the manifolds associated with the TS.[57,60,61] The values of these LDs diverge on either side of a phase space boundary separating distinct dynamical basins. These special boundaries are manifolds and they are distinguished by drastic changes in the derivative of M and correspond to local minima on the M surface.

The LD corresponding to the arc length projection in configuration space is

$$L(\mathbf{q}_0, t_0)_\tau = \int_{t_0-\tau}^{t_0+\tau} \|\dot{\mathbf{q}}_c(\mathbf{q}_0, t_0, t)\|\mathrm{d}t, \quad (9)$$

where $\mathbf{q}_c$ is a set of generalized coordinates and $\|\cdot\|$ is the norm. Thus, L is a measure of the distance traveled in configuration space over the time interval $[t_0 - \tau, t_0 + \tau]$ by the trajectory that passes through the phase space point $\mathbf{q}_0$ at time t_0. This LD can be separated into forward-time

$$L_f(\mathbf{q}_0, t_0)_\tau = \int_{t_0}^{t_0+\tau} \|\dot{\mathbf{q}}_c(\mathbf{q}_0, t_0, t)\|\mathrm{d}t, \quad (10)$$

and backward-time

$$L_b(\mathbf{q}_0, t_0)_\tau = \int_{t_0-\tau}^{t_0} \|\dot{\mathbf{q}}_c(\mathbf{q}_0, t_0, t)\| dt, \quad (11)$$

components by integrating in the respective time direction. The value of τ is chosen to be long enough such that distinct features are observed on the LD surfaces. Note that the initial conditions of each trajectory $\mathbf{q}_0(t_0) = (q_1(t_0),\dot{q}_1(t_0),q_2(t_0),\dot{q}_2(t_0))$ are phase space coordinates, while the integration of these LDs is performed over projections into configuration space. We use eqn (9)–(11) below to describe the geometry of ketene isomerization.

With the inclusion of field–dipole coupling, the system of eqn (7a) and (7b) becomes time-dependent. The stationary transition states (see Table 2) now become time-dependent and generate a set of stable manifolds W^s, unstable manifolds W^u, and corresponding hyperbolic trajectories. The manifolds associated with each moving TS are also time-dependent. The direct construction of these objects can provide physical insight into the mechanism and nature of reactions in which moving energy barriers separate reactant and product states. The LD procedure, requiring forward and backward integration in time, thus provides information on how the past reaction geometry (described by the manifold network) evolves into the future geometry in these time-dependent flows.

The two models summarized in Section 1 contain distinct topology due to differences in dimensionality. The complexity of the dynamics that occur in these topological spaces can be reduced by considering different sets of phase spaces and phase planes in which to perform the LD analysis. Model I has a single degree of freedom and its dynamics occur solely on the principal reaction coordinate q_1 and the corresponding $q_1 \times \dot{q}_1$ phase space. The measure of eqn (9)–(11) in Model I is taken over q_1 as it is the only configuration space component. The addition of a second degree of freedom q_2 in Model II leads to the generation of additional planes in phase space, *e.g.*, $q_2 \times \dot{q}_2$ and configuration space $q_1 \times q_2$. While other spaces exist, we find these planes as the most intuitive and pertinent in which to perform analysis. Alternatively, the complex reaction dynamics in systems with high dimensionality is often simplified by identifying suitable collective variable reaction coordinates and performing analysis within a reduced space. In Model II, we therefore consider LDs constructed using the arc length measure over q_1 space alone, as it is the putative reaction coordinate. This reductionist approach is particularly advantageous for chemical reactions addressed through LD analysis because the dynamics in the nonreactive modes play only a secondary role in activated events.

3 Dynamics

We first consider an autonomous model of ketene isomerization by removing the driving field (*i.e.* $\mathscr{E}_0 = 0.0$). In this system, the TS saddle points are connected by a network of heteroclinic and homoclinic loops. The heteroclinic loops consist of trajectories that approach different TSs in the infinite past and future. Homoclinic loops are made up of trajectories that approach the same TS in forward and backward time. These loops correspond to the stable (unstable in backward time) manifold for a given saddle point TS_i and are denoted as

$$\underset{i\to j}{W}(TS_i) \quad \text{and} \quad \underset{i\to i}{W}(TS_i)$$

respectively. The notation $i \to j$ signifies the heteroclinic connection from TS_i to TS_j and $i \to i$ signifies a homoclinic connection. Note that in backward time, the direction of the $i \to j$ connection is $j \to i$. These manifolds can be constructed by holding q_1 constant while minimizing the LD with respect to $\dot{q}_1$, and/or finding the corresponding points where the derivative of the LD changes "abruptly."[57,60] The manifolds are clearly visible in the top panel of Fig. 2 as strong local minima on the L surface and the power of LDs is evident as the manifold structure in forward and backward time are revealed.

In this autonomous system, trajectories with initial conditions on hyperbolic fixed points result in $L_f = 0$, $L_b = 0$, and $L = 0$ by definition, and these points correspond to TS saddle points.

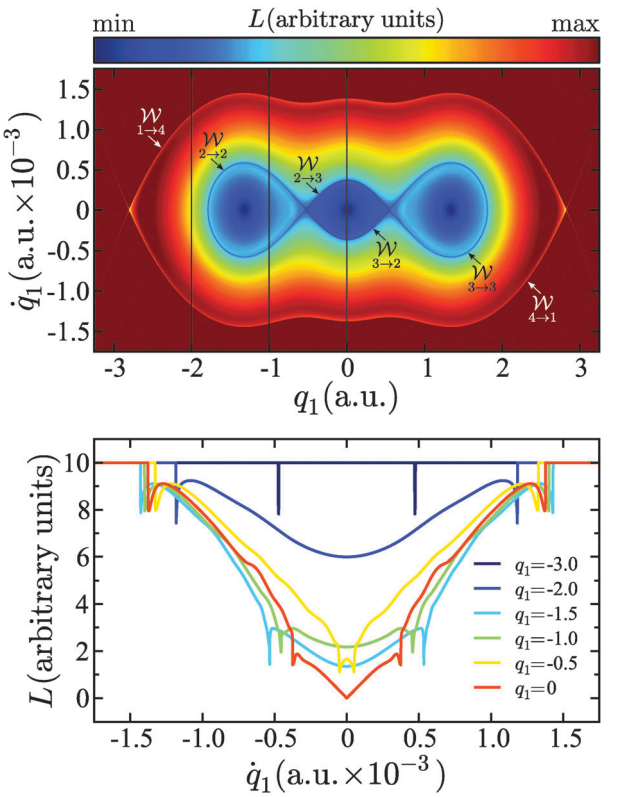

Fig. 2 (top) A contour plot of the Lagrangian surface L for autonomous ($\mathscr{E}_0 = 0.0$) ketene isomerization in $q_1 \times \dot{q}_1$ space. The heteroclinic and homoclinic loops are marked as discussed in the text and correspond to distinctive features on L. (bottom) The values of L along the constant values of q_1 given in the legend. The location of the slices corresponding to $q_1 \in \{-2.0, -1.0, 0\}$ are shown as solid black lines in the top panel. All parameter values are given in atomic units. For visual clarity in this and all other figures illustrating LD surfaces, a threshold value limits the upper bound of L and corresponds to the "max" value shown in the deepest red.

All other trajectories with initial conditions not on TS_t saddle points have LDs with positive values such that finding the minima allows locating the TSs. This behavior is illustrated by the $q_1 = 0$ curve in Fig. 2. The stable manifolds of these TSs can be constructed by considering forward-time integration only. For a chosen initial position (that is held constant), varying the initial velocity leads to trajectories with two different behaviors: those that are not on the stable manifold move away from the TS (sliding down the barrier) and thus have large values of L_f over sufficient propagation. However, on this line of constant initial position, there is one initial velocity that gives a trajectory that approaches the TS, remaining bounded for all time. This trajectory belongs to the stable manifold and will have the minimum value of L_f, as it never descends from the region of the barrier top into the metastable energy wells. The unstable manifold can be constructed using similar arguments on the L_b surface, and backwards-time integration. In the bottom panel of Fig. 2, it can be seen that the stable (unstable) manifold of each TS exhibits distinctive features on the L surface.

Upon inclusion of the external driving field, the network of manifolds becomes time-dependent. As shown in Fig. 3, this network exhibits oscillatory motion due to the periodicity in the driving form. The homoclinic and hetereoclinic loops associated with each TS persist, albeit in a time-varying form. This persistence would cease upon inclusion of dissipative forces, such as those experienced by a reactive species in a solvent environment. They do not however require periodic driving as the arguments for uncovering the manifolds and TS using LDs did not rest on this assumption. This opens the possibility for addressing aperiodic driving forms, *e.g.*, thermal fluctuations, with the LD approach, and the resulting alterations in the reactive yields in chemical reactions.

At select values of field strength and oscillation frequency ($\varepsilon_0 = 0.03$ a.u. and $\omega = 0.0025$ a.u.), the onset of chaos is observed as characterized by complex stretching and contracting behavior in phase space leading to entanglement of the stable and unstable manifolds. This behavior can be seen in Fig. 4. At these field parameters, a bifurcation threshold has been crossed due to the appearance of additional hyperbolic points connected by stable and unstable manifolds. While rigorous analysis of this complex structure is beyond the scope of this manuscript, formalisms have been developed to understand the induced phase space partitioning.[77,78] Using the method of LDs, the complexity of this network can be simplified by constructing both the L_f and L_b surfaces and subsequent analysis of the dynamics in the respective time direction separately. As shown in Fig. 5, on these unidirectional time surfaces, the corresponding stable and unstable manifolds are visible as distinctive features in the relevant phase space regions. Moreover, the constructed surfaces L_f and L_b reveal the encapsulated reactive (nonreactive) islands dictating the flow from reactant to product. This method can be applied directly to ketene isomerization with other field parameters, and, most importantly, to other general chemical reactions, to understand how the network of manifolds, and the corresponding reaction dynamics, are affected by an applied field.

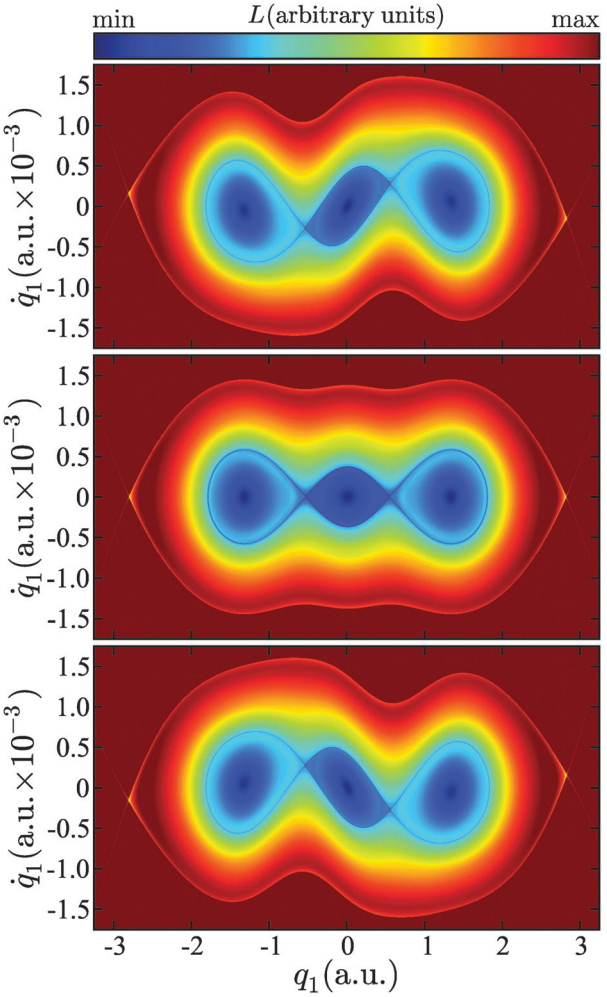

Fig. 3 Contour plots of the Lagrangian surface L for field-induced ketene isomerization (Model I) in $q_1 \times \dot{q}_1$ space with $\mathscr{E}_0 = 0.5$, $\omega = 0.0315$, $\tau = 10^3$, for $t_0 = 0$ (top), $t_0 = 75$ (middle), and $t_0 = 100$ (bottom). All parameter values are given in atomic units.

Multidimensional reactive systems can also be analyzed using the LD method. In Model II of Section 1, the out-of-plane motion of the H atom in oxirene is a second degree of freedom (q_2) that complements the dynamics on principal reaction coordinate q_1. The dynamics in these two coordinates are coupled through the potential energy term given by eqn (4). Following the multidimensional study of ketene isomerization rates by Gezelter and Miller in ref. 72, Ulusoy and Hernandez,[62–64] and also Mauguière *et al.*,[65] used the GM model to examine the dynamics of ketene in a phase space perspective. In the multidimensional space, with inclusion of field-matter interactions, the onset of chaotic behavior can also be observed. As shown in Fig. 6, phase planes containing trajectories with higher initial energy result in more dissociative-type transformations as the yield of ketene (dark red) increases. This general trend persists with increasing initial velocity in q_1. The origin of this behavior is that larger values of $\dot{q}_1(t_0)$ increase the initial energy of each trajectory. Thus, the likelihood of a trajectory escaping from the intermediate oxirene and formylmethylene metastable wells is also increased

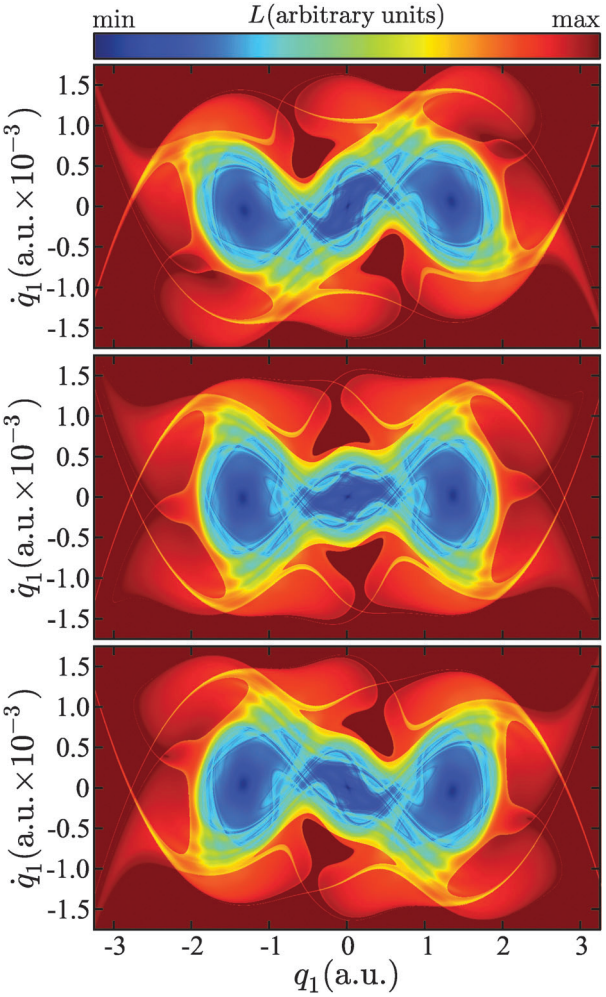

Fig. 4 Contour plots of the Lagrangian surface L for field-induced ketene isomerization (Model I) in $q_1 \times \dot{q}_1$ space with $\mathscr{E}_0 = 0.03$, $\omega = 0.0025$, and $\tau = 10^3$, for $t_0 = 0$ (top), $t_0 = 500$ (middle), and $t_0 = 1000$ (bottom). All parameter values are given in atomic units.

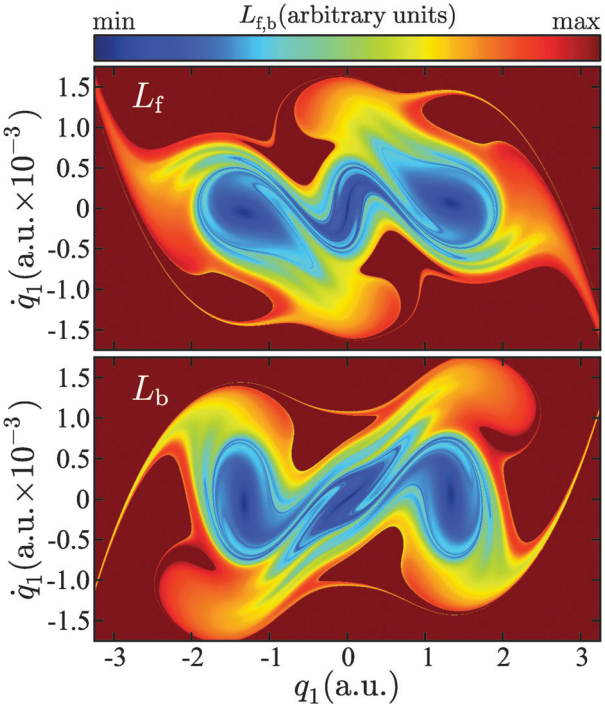

Fig. 5 Contour plots of the forward-time (top) and backward-time (bottom) Lagrangian surfaces $L_{f,b}$ in $q_1 \times \dot{q}_1$ space for Model I with $\mathscr{E}_0 = 0.03$, $\omega = 0.0025$, $\tau = 10^3$, and $t_0 = 0$. All parameter values are given in atomic units.

as energy from the velocity space is transferred into the reaction coordinate. Note the measure of L_f is taken over q_1 only. Although not shown, we also observed improved ketene yields with increasing q_2 and $\dot{q}_2$. In this case, the energy transfer into q_1 occurs through coupling on the potential energy surface.

4 Reactivity and final-state basins

The reactivity and selectivity of ketene isomerization, dynamically modeled through eqn (7a) and (7b), can be examined by mapping initial conditions in phase space to the corresponding final state basin. This procedure involves taking a set of coordinates in the multidimensional phase space as the initial condition for the equations of motion, and following the evolution of trajectories to some final time in order to determine what regions in phase space lead to which products. A large number of trajectories are often necessary in order to adequately sample the basin boundaries as initial conditions are, most commonly, generated using an equally-spaced grid. Creating the mapping from phase space points to final states is analogous to the brute-force computation of basins of attraction in dynamical systems.

For the models of ketene isomerization defined in Section 1, we can identify five stable state regions separated by TSs on the GM energy surface. The one-dimensional coordinate q_1 parameterizes the curved reaction coordinate well and can serve as an indicator of the final state as illustrated in Fig. 1. A mapping of each position $\mathbf{q}_0$ to a given final state S_k can thus be constructed through an indicator function

$$S(\mathbf{q}_0(t_0),\tau) = \begin{cases} S_1, & q_1(\tau) < \mathrm{TS}_1, \\ S_2, & q_1(\tau) > \mathrm{TS}_1 \text{ and } q_1(\tau) < \mathrm{TS}_2, \\ S_3, & q_1(\tau) > \mathrm{TS}_2 \text{ and } q_1(\tau) < \mathrm{TS}_3, \\ S_4, & q_1(\tau) > \mathrm{TS}_3 \text{ and } q_1(\tau) < \mathrm{TS}_4, \\ S_5, & q_1(\tau) > \mathrm{TS}_4, \end{cases} \quad (12)$$

according to the location of the final position of the q_1-mode of the trajectory $\mathbf{q}_0(\tau)$.

For Model I, the state mapping encoded by eqn (12) is shown in Fig. 7 over various parameter values of the driving field and increasing integration times. Only forward-time integration is considered, and thus the reactive regions will be separated by stable manifolds of the TSs. In the nonchaotic regimes of Fig. 7(a) and (b), the we observe an the regular structure seen earlier for the manifolds obtained using LDs. In Fig. 7(c), the reactive islands observed through direct calculation of the final state basins are seen to correspond to regions enclosed by the same stable manifolds observed on the forward-time LD

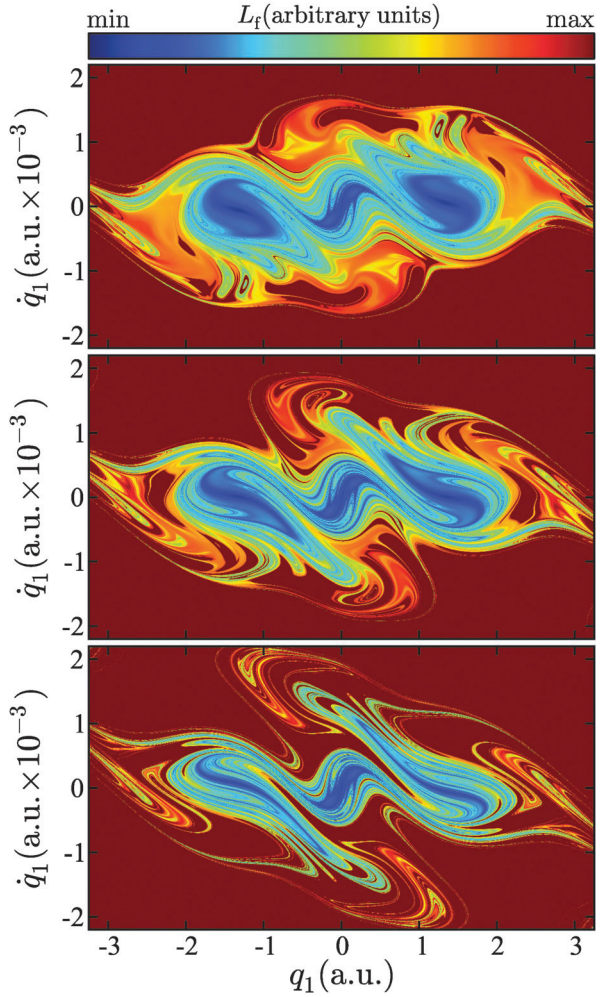

Fig. 6 Contour plots of the Lagrangian surface L_f for field-induced ketene isomerization (Model II) in $q_1 \times \dot{q}_1$ space with $\mathscr{E}_0 = 0.03$, $\omega = 0.0025$, $\tau = 2.5 \times 10^3$, and $q_2(t_0) = 0$ for $\dot{q}_2(t_0) = 0$ (top), $\dot{q}_2(t_0) = 0.001$ (middle), and $\dot{q}_2(t_0) = 0.002$ (bottom) with $t_0 = 0$. The measure of L_f is taken over q_1 space. All parameter values are given in atomic units.

surface L_f in Fig. 5. Also note that in Fig. 7(c) there is clear evidence of chaotic mixing which was previously posited using information from the LD surface only. As shown in all panels in Fig. 6 corresponding to integration times $\tau = 10^3$ a.u., the stable manifold network, calculated using the method of LDs described in Section 2, is in excellent agreement with boundaries that separate regions of different selectivity. This result illustrates that the manifold network dictating reactivity in chemical reactions can be exposed using LDs.

Final state probabilities $P(S_k)$ for several parameter ranges in Model I are shown in Fig. 8(a)–(c). These probabilities are calculated by counting the fraction of trajectories starting in region $\mathscr{R} = [-3.6 \text{ a.u.}, 3.6 \text{ a.u.}] \times [-0.0022 \text{ a.u.}, 0.0022 \text{ a.u.}]$ in phase space that lead to the final states S_k for $k \in \{1, 2, 3, 4, 5\}$ according to the mapping in eqn (12). In Fig. 8(a), the reaction probabilities for the field strength $\mathscr{E}_0 = 1.0$ a.u. are illustrated over varying frequencies. A distinct turnover regime in which oxirene is favored over formylmethylene is observed over the frequencies $\omega \in [1 \text{ a.u.} \times 10^{-5}, 2.5 \text{ a.u.} \times 10^{-5}]$ and also for $\omega \in [7 \text{ a.u.} \times 10^{-5}, 9 \text{ a.u.} \times 10^{-5}]$. Fig. 8(b) illustrates reaction probabilities for a reduced field intensity $\mathscr{E}_0 = 0.2$ a.u. over the frequency regime $[1 \text{ a.u.} \times 10^{-3}, 1 \text{ a.u.} \times 10^{-2}]$. For this field strength and frequency $\omega = 0.001$ a.u., almost all trajectories lead to the production of ketene. At an order of magnitude larger frequency ($\omega = 0.01$ a.u.), the yields of the autonomous system are approached. As shown in Fig. 8(c), increasing the field strength while holding the frequency constant at $\omega = 0.0025$ a.u. leads to monotonically increasing yields of ketene. Note that as $\mathscr{E}_0 \to 0$, the final state probabilities for the autonomous system are recovered.

The final state mapping procedure can also be performed in multidimensional dynamical systems. In the case of ketene isomerization represented by Model II, the configuration space $q_1 \times q_2$ is two-dimensional and trajectories evolve on the potential energy surface shown in the bottom panel of Fig. 1. The LD method allows examination of multidimensional dynamics and verification of the constructed phase space boundaries by comparison to the final state basin mappings. It can also be used to provide qualitative information about a reactive system, such as the location of strong gradients which lead to regions corresponding to state transitions. As illustrated in Fig. 9, the same general trends are observed in configuration space as were observed in the principal phase space $q_1 \times \dot{q}_1$ insofar as phase planes containing trajectories with larger initial kinetic energies lead to increased ketene production. This general trend can also be observed in Fig. 8(d) where it is shown that increasing the initial velocity $\dot{q}(t_0)$ in the principal reaction coordinate leads to the production of more ketene, and thus larger values of $P(S_1)$ and $P(S_5)$. Comparisons of the forward-time LD surface (L_f) and final state basin mapping for both autonomous and field-driven ketene isomerization are shown in Fig. 9 and 10, respectively. Over the parameters values studied, the complexity of the final-state basin mapping is recovered using LDs, that is, the L_f surface almost perfectly mimics the S mapping. The results from these calculations imply that the physical insight gained from the LD method is highly dependent on the geometry of the potential energy surface, driving form, and system dimensionality. Due to generality in the formulation and the complexity of the underlying model of ketene, we expect that the general trends observed here will persist in other chemical reactions and other classes of activated events.

The existence of boundaries where the LD measure changes quickly from areas of small arc length (dark blue) to large arc length (dark red) in Fig. 9 and 10 may correspond to alternative pathways in the reaction dynamics. We conjecture that these transitions correspond to encapsulated regions of roaming trajectories: trajectories that move from a reactant state to a product state without nearing the bottleneck region (the canonical transition state) in phase space. In the present case, trajectories in these regions satisfy at least one of the roaming criteria[62] by exhibiting drastically different dynamical behavior across boundaries. What is difficult to discern from these results and we leave to future work is whether they satisfy some of the other requirements associated with roaming trajectories. Ulusoy and

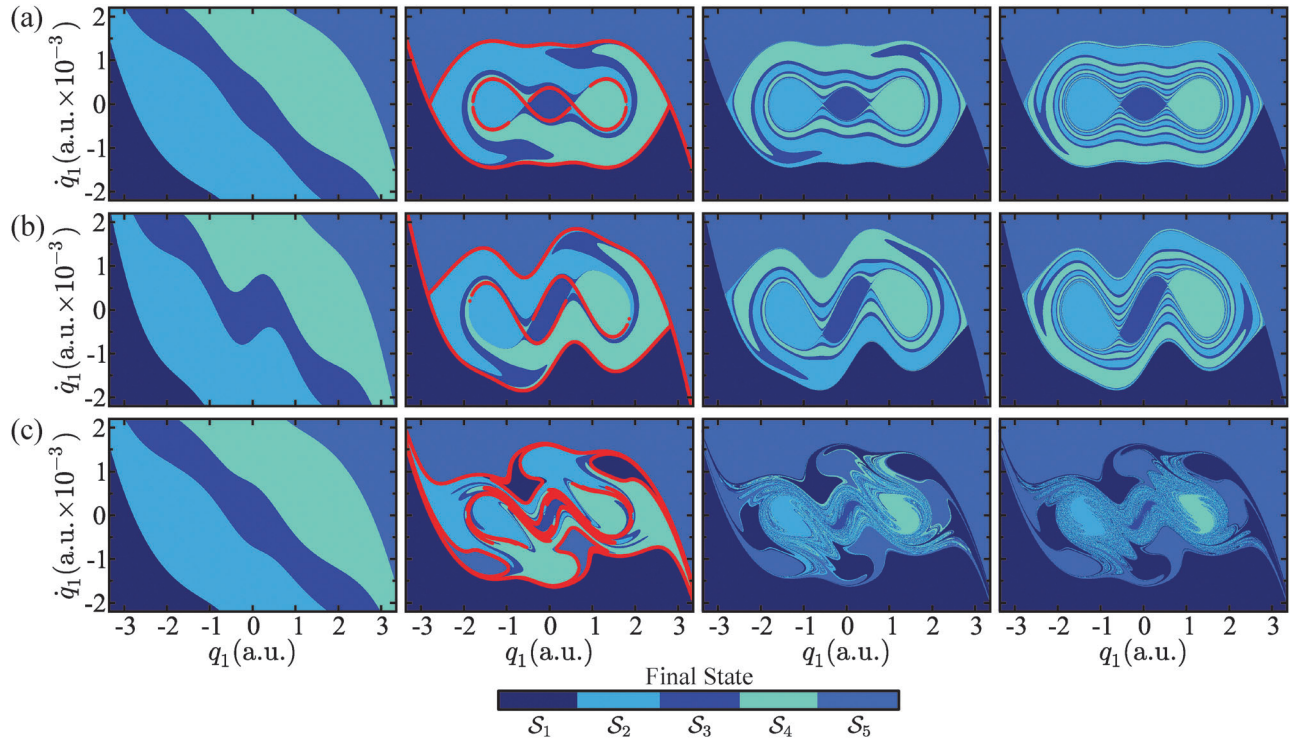

Fig. 7 Final state basins in $q_1 \times \dot{q}_1$ space for Model I and (a) ($\mathscr{E}_0 = 0$), (b) ($\mathscr{E}_0 = 1.0$, $\omega = 0.0315$), and (c) ($\mathscr{E}_0 = 0.03$, $\omega = 0.0025$). The initial time is $t_0 = 0$ in all panels. From left to right, the integration times are $\tau \in \{10^3, 10^4, 2.5 \times 10^4, 5.0 \times 10^4\}$. In all panels corresponding to $\tau = 10^4$, pieces of the stable manifold network, as calculated using the method of LDs described in Section 2, are shown in red. All parameters values are given in atomic units.

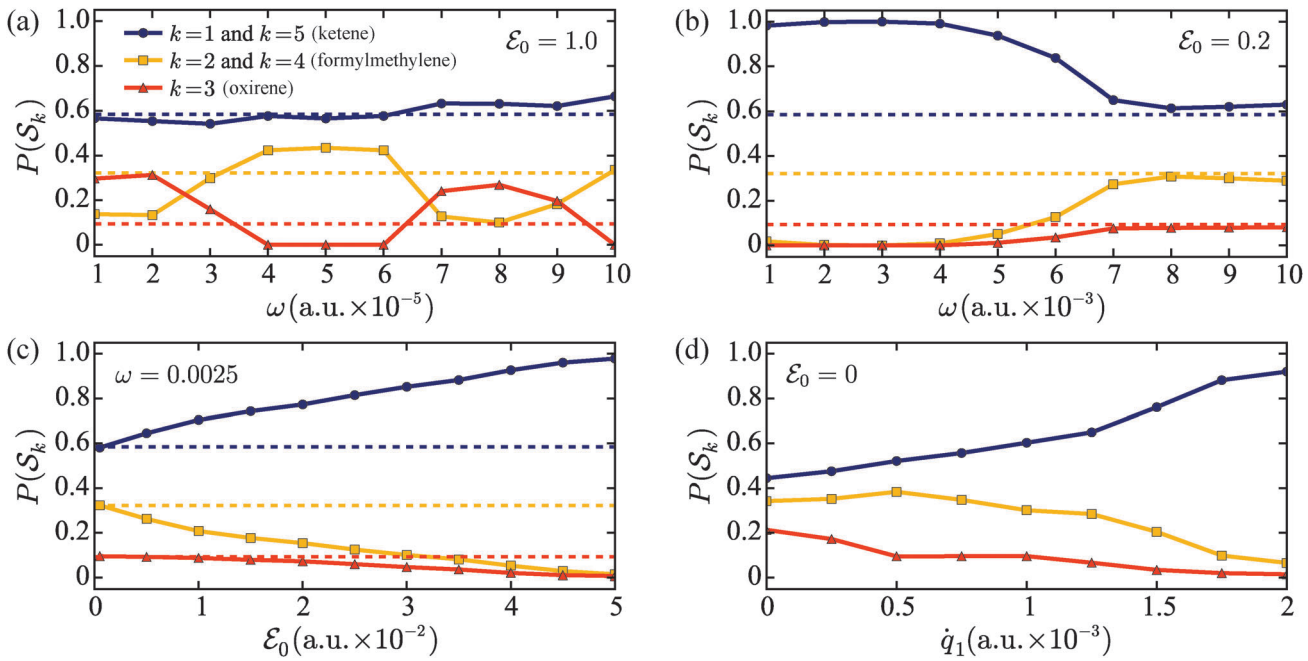

Fig. 8 Final state probabilities $P(S_k)$ for Model I with: (a) $\mathscr{E}_0 = 1.0$ and (b) $\mathscr{E}_0 = 0.2$, while varying ω, and (c) $\omega = 0.0025$ while varying $\mathscr{E}_0$, as measured over the region $[-3.6, 3.6] \times [-0.0022, 0.0022]$ in $q_1 \times \dot{q}_1$ space. The dashed lines correspond to probabilities for the respective states in an autonomous ($\mathscr{E}_0 = 0$) system. (d) Final state probabilities measured in the $q_1 \times q_2$ plane over region $[-3.6, 3.6] \times [-3.6, 3.6]$ for Model II with $\dot{q}_2(t_0) = 0$ and $\mathscr{E}_0 = 0$ while varying the initial condition $\dot{q}_1(t_0)$. In all panels $t_0 = 0$ and $\tau = 10^5$. All parameters values are given in atomic units.

Hernandez investigated this phenomena in autonomous ketene isomerization using classical calculations on the GM surface and found these types of trajectories exist, but do not contribute significantly to the isomerization reaction rate.

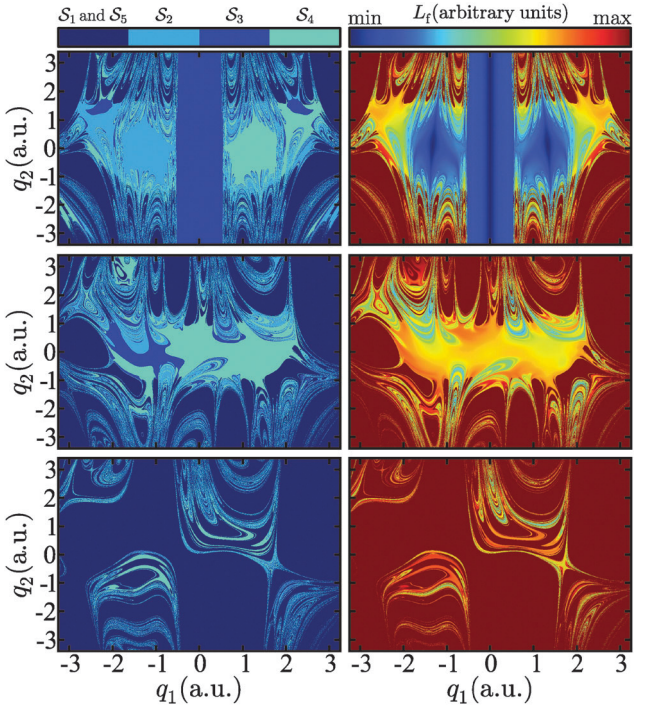

Fig. 9 Final state basins (left) and contour plots of L_f (right) in $q_1 \times q_2$ space for autonomous ketene isomerization (Model II). The initial velocities are (top) $\dot{q}_1(t_0) = 0.0$, (middle) $\dot{q}_1(t_0) = 0.001$, and (bottom) $\dot{q}_1(t_0) = 1.5 \times 10^{-3}$, with $\dot{q}_2(t_0) = 0$ in all panels. Other parameters are $\mathscr{E}_0 = 0$, $\tau = 2.5 \times 10^3$, and $t_0 = 0$. The measure of L_f is taken over q_1 space. All parameter values are given in atomic units.

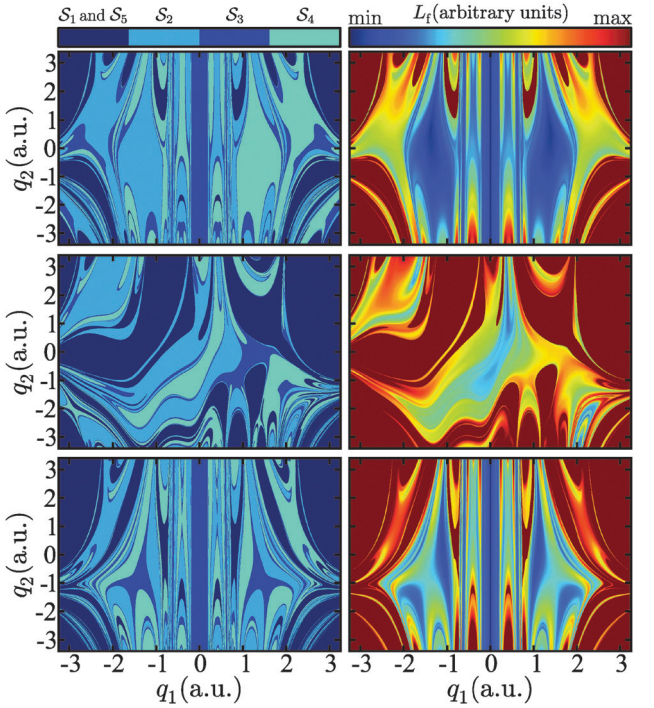

Fig. 10 Final state basins (left) and contour plots of L_f (right) in $q_1 \times q_2$ space for Model II with (top) $\dot{q}_1(t_0) = \dot{q}_2(t_0) = 0$, (middle) $\dot{q}_1(t_0) = \dot{q}_2(t_0) = 0.001$, (bottom) $\dot{q}_1(t_0) = 0$ and $\dot{q}_2(t_0) = 0.003$. Parameters are $\mathscr{E}_0 = 0.03$, $\omega = 0.0025$, $\tau = 10^3$, and $t_0 = 0$. The measure of L_f is taken over q_1 space. All parameter values are given in atomic units.

Mauguière *et al.*[65,79,80] gave further analysis by computing gap-time distributions, and also counting the number of times trajectories cross dividing surfaces in phase space. They concluded that a trajectory could be quantified as roaming depending on the number of crossings. As a rigorous dynamical formulation of roaming is nascent, a possible direction of future research is to examine this phenomena using LDs. While a full description of the existence and characterization of roaming is beyond the scope of this manuscript, investigations are currently underway to describe this mechanism in field-induced ketene isomerization and other reactions.

5 Conclusions

The isomerization of ketene has been characterized using a reduced-dimensional dynamical model and the method of Lagrangian descriptors. The reactive system has been modeled through the Gezelter–Miller potential energy surface and a molecular dipole moment approximation, with both constructed from *ab initio* calculations. We have examined the time-dependent stable and unstable manifolds in field-induced ketene isomerization over varying field strengths and field oscillation frequencies. These manifolds encapsulate subregions in phase space (and configuration space) that correspond to the formation of different products. We found that phase space separatrices dictating state transitions can be constructed in field-induced chemical reactions thereby revealing the underlying reactions mechanisms. Although we have considered a periodically driven system, the methods do not rely on periodicity for implementation and can be applied in aperiodic fields and other driving forms, such as thermal environments, with no loss of generality. One possible application of the presented methodology is to predict the reactivity and selectivity of chemical reactions over varying field shapes, envelopes, and field strengths. The formalism developed here allows for prediction of reaction geometries in processes occurring in complex environments, including general stimuli-responsive phenomena.

Acknowledgements

This work has been partially supported by the Air Force Office of Scientific Research through Grant No. FA9550-12-1-0483. GTC thanks Abraham Nitzan and the Department of Chemistry at the University of Pennsylvania for support and hospitality during the latter stages of preparation.

References

1 D. G. Truhlar and B. C. Garrett, *Annu. Rev. Phys. Chem.*, 1984, **35**, 159–189.
2 W. H. Miller, *Acc. Chem. Res.*, 1993, **26**, 174.
3 D. G. Truhlar, B. C. Garrett and S. J. Klippenstein, *J. Phys. Chem.*, 1996, **100**, 12771–12800.
4 T. Komatsuzaki and R. S. Berry, *Proc. Natl. Acad. Sci. U. S. A.*, 2001, **98**, 7666–7671.

5 H. Waalkens, R. Schubert and S. Wiggins, *Nonlinearity*, 2008, **21**, R1.
6 T. Bartsch, J. M. Moix, R. Hernandez, S. Kawai and T. Uzer, *Adv. Chem. Phys.*, 2008, **140**, 191–238.
7 S. Kawai and T. Komatsuzaki, *Phys. Rev. Lett.*, 2010, **105**, 048304.
8 R. Hernandez, T. Bartsch and T. Uzer, *Chem. Phys.*, 2010, **370**, 270–276.
9 E. Pollak and P. Pechukas, *J. Chem. Phys.*, 1978, **69**, 1218–1226.
10 E. Pollak and P. Pechukas, *J. Chem. Phys.*, 1979, **70**, 325–333.
11 P. Pechukas and E. Pollak, *J. Chem. Phys.*, 1979, **71**, 2062–2068.
12 E. Pollak, M. S. Child and P. Pechukas, *J. Chem. Phys.*, 1980, **72**, 1669.
13 R. Hernandez and W. H. Miller, *Chem. Phys. Lett.*, 1993, **214**, 129–136.
14 R. Hernandez, *J. Chem. Phys.*, 1994, **101**, 9534–9547.
15 T. Uzer, C. Jaffé, J. Palacián, P. Yanguas and S. Wiggins, *Nonlinearity*, 2002, **15**, 957–992.
16 N. De Leon, M. A. Mehta and R. Q. Topper, *J. Chem. Phys.*, 1991, **94**, 8310–8328.
17 C.-B. Li, A. Shoujiguchi, M. Toda and T. Komatsuzaki, *Phys. Rev. Lett.*, 2006, **97**, 028302.
18 H. Waalkens and S. Wiggins, *J. Phys. A: Math. Theor.*, 2004, **37**, L435–L445.
19 G. S. Ezra, H. Waalkens and S. Wiggins, *J. Chem. Phys.*, 2009, **130**, 164118.
20 G. S. Ezra and S. Wiggins, *J. Phys. A: Math. Theor.*, 2009, **42**, 205101.
21 H. Teramoto, M. Toda and T. Komatsuzaki, *Phys. Rev. Lett.*, 2011, **106**, 054101.
22 M. Iñarrea, J. F. Palacián, A. I. Pascual and J. P. Salas, *J. Chem. Phys.*, 2011, **135**, 014110.
23 A. Allahem and T. Bartsch, *J. Chem. Phys.*, 2012, **137**, 214310.
24 R. S. MacKay and D. C. Strub, *Nonlinearity*, 2014, **27**, 859.
25 H. Teramoto, M. Toda, M. Takahashi, H. Kono and T. Komatsuzaki, *Phys. Rev. Lett.*, 2015, **115**, 093003.
26 J. Guckenheimer, B. Krauskopf, H. M. Osinga and B. Sandstede, *Chaos*, 2015, **25**, 097604.
27 Z. C. Kramer, B. K. Carpenter, G. S. Ezra and S. Wiggins, *J. Phys. Chem. A*, 2015, **119**, 6611–6630.
28 T. Bartsch, R. Hernandez and T. Uzer, *Phys. Rev. Lett.*, 2005, **95**, 058301.
29 T. Bartsch, T. Uzer and R. Hernandez, *J. Chem. Phys.*, 2005, **123**, 204102.
30 T. Bartsch, T. Uzer, J. M. Moix and R. Hernandez, *J. Chem. Phys.*, 2006, **124**, 244310.
31 G. E. Murgida, D. A. Wisniacki, P. I. Tamborenea and F. Borondo, *Chem. Phys. Lett.*, 2010, **496**, 356–361.
32 G. T. Craven, T. Bartsch and R. Hernandez, *Phys. Rev. E: Stat., Nonlinear, Soft Matter Phys.*, 2014, **89**, 040801.
33 G. T. Craven, T. Bartsch and R. Hernandez, *J. Chem. Phys.*, 2014, **141**, 041106.
34 G. T. Craven, T. Bartsch and R. Hernandez, *J. Chem. Phys.*, 2015, **142**, 074108.
35 M. Canadell and R. de la Llave, *Phys. D*, 2015, **310**, 104–113.
36 S. Kawai, A. D. Bandrauk, C. Jaffé, T. Bartsch, J. Palacián and T. Uzer, *J. Chem. Phys.*, 2007, **126**, 164306.
37 S. Kawai and T. Komatsuzaki, *J. Chem. Phys.*, 2011, **134**, 024317.
38 D. Blazevski and R. de la Llave, *J. Phys. A: Math. Theor.*, 2011, **44**, 195101.
39 D. Blazevski and J. Franklin, *Chaos*, 2012, **22**, 043138.
40 F. Revuelta, T. Bartsch, R. M. Benito and F. Borondo, *J. Chem. Phys.*, 2012, **136**, 091102.
41 T. Bartsch, F. Revuelta, R. M. Benito and F. Borondo, *J. Chem. Phys.*, 2012, **136**, 224510.
42 A. Sethi and S. Keshavamurthy, *Phys. Rev. A: At., Mol., Opt. Phys.*, 2009, **79**, 033416.
43 S. Patra and S. Keshavamurthy, *Chem. Phys. Lett.*, 2015, **634**, 1–10.
44 F. Revuelta, R. Chacón and F. Borondo, *Europhys. Lett.*, 2015, **110**, 40007.
45 R. Q. Topper, *Rev. Comput. Chem.*, 1997, **10**, 101.
46 S. W. Flynn, H. C. Zhao and J. R. Green, *J. Chem. Phys.*, 2014, **141**, 104107.
47 J. W. Nichols, S. W. Flynn and J. R. Green, *J. Chem. Phys.*, 2015, **142**, 064113.
48 P. Cvitanović, R. Artuso, R. Mainieri, G. Tanner and G. Vattay, *Chaos: Classical and Quantum*, ChaosBook.org, Niels Bohr Institute, Copenhagen, 2012.
49 C. Skokos, *Phys. D*, 2001, **159**, 155–179.
50 R. P. Boland, T. Galla and A. J. McKane, *Phys. Rev. E: Stat., Nonlinear, Soft Matter Phys.*, 2009, **79**, 051131.
51 F. L. Traversa, M. Di Ventra and F. Bonani, *Phys. Rev. Lett.*, 2013, **110**, 170602.
52 L. P. Kadanoff and C. Tang, *Proc. Natl. Acad. Sci. U. S. A.*, 1984, **81**, 1276–1279.
53 R. T. Skodje and M. J. Davis, *Chem. Phys. Lett.*, 1990, **175**, 92–100.
54 H. Gelman, M. Platkov and M. Gruebele, *Chem. – Eur. J.*, 2012, **18**, 6420–6427.
55 M. Platkov and M. Gruebele, *J. Chem. Phys.*, 2014, **141**, 035103.
56 J. Morfill, J. Neumann, K. Blank, U. Steinbach, E. M. Puchner, K.-E. Gottschalk and H. E. Gaub, *J. Mol. Biol.*, 2008, **381**, 1253–1266.
57 C. Mendoza and A. M. Mancho, *Phys. Rev. Lett.*, 2010, **105**, 038501.
58 J. A. Jiménez Madrid and A. M. Mancho, *Chaos*, 2009, **19**, 013111.
59 S. Balasuriya and K. Padberg-Gehle, *Phys. Rev. E: Stat., Nonlinear, Soft Matter Phys.*, 2014, **90**, 032903.
60 A. M. Mancho, S. Wiggins, J. Curbelo and C. Mendoza, *Commun. Nonlinear Sci. Numer. Simul.*, 2013, **18**, 3530–3557.
61 G. T. Craven and R. Hernandez, *Phys. Rev. Lett.*, 2015, **115**, 148301.
62 I. S. Ulusoy, J. F. Stanton and R. Hernandez, *J. Phys. Chem. A*, 2013, **117**, 7553–7560.
63 I. S. Ulusoy, J. F. Stanton and R. Hernandez, *J. Phys. Chem. A*, 2013, **117**, 10567.
64 I. S. Ulusoy and R. Hernandez, *Theor. Chem. Acc.*, 2014, **133**, 1528.

65 F. A. L. Maugière, P. Collins, G. Ezra, S. C. Farantos and S. Wiggins, *Theor. Chim. Acta*, 2014, **133**, 1507.
66 E. R. Lovejoy, S. K. Kim and C. B. Moore, *Science*, 1992, **256**, 1541–1544.
67 S. K. Kim, E. R. Lovejoy and C. B. Moore, *J. Chem. Phys.*, 1995, **102**, 3202–3219.
68 A. P. Scott, R. H. Nobes, H. F. Schaefer III and L. Radom, *J. Am. Chem. Soc.*, 1994, **116**, 10159–10164.
69 J. Ferrero and G. Arbilla, *Chem. Phys. Lett.*, 1991, **187**, 613–618.
70 M. Castillejo, S. Couris, E. Lane, M. Martin and J. Ruiz, *Comput. Phys.*, 1998, **232**, 353–360.
71 J. Fenwick, G. Frater, K. Ogi and O. P. Strausz, *J. Am. Chem. Soc.*, 1973, **95**, 124–132.
72 J. D. Gezelter and W. H. Miller, *J. Chem. Phys.*, 1995, **103**, 7868–7876.
73 B. N. Hannay and C. P. Smyth, *J. Am. Chem. Soc.*, 1946, **68**, 1357–1360.
74 B. Fabricant, D. Krieger and J. S. Muenter, *J. Chem. Phys.*, 1977, **67**, 1576–1586.
75 J. D. Farnum and D. A. Mazziotti, *Chem. Phys. Lett.*, 2005, **416**, 142–146.
76 E. Acar, T. Senst, A. Kuhn, I. Keller, H. Theisel, S. Albayrak and T. Sikora, IEEE, 14th International Workshop on Multimedia Signal Processing (MMSP), 2012, pp. 360–365.
77 K. A. Mitchell, *Phys. D*, 2009, **238**, 737–763.
78 K. A. Mitchell, *Phys. D*, 2012, **241**, 1718–1734.
79 F. A. L. Maugière, P. Collins, G. Ezra, S. C. Farantos and S. Wiggins, *Chem. Phys. Lett.*, 2014, **592**, 282–287.
80 F. A. L. Maugière, P. Collins, G. Ezra, S. C. Farantos and S. Wiggins, *J. Chem. Phys.*, 2014, **140**, 134112.

